Mechatronics 39 (2016) 1–11

Contents lists available at ScienceDirect

Mechatronics

journal homepage: www.elsevier.com/locate/mechatronics

Optimized estimator for real-time dynamic displacement measurement using accelerometers

Jonathan Abir[a,*], Stefano Longo[b], Paul Morantz[a], Paul Shore[c]

[a] The Precision Engineering Institute, School of Aerospace, Transport and Manufacturing, Cranfield University, Cranfield, MK43 0AL, UK
[b] The Centre for Automotive Engineering and Technology, Cranfield University, Cranfield, MK43 0AL, UK
[c] The National Physical Laboratory, Teddington, TW11 0LW, UK

ARTICLE INFO

Article history:
Received 19 May 2016
Revised 11 July 2016
Accepted 22 July 2016

Keywords:
Accelerometer
Displacement estimation
Flexible frame
Heave filter
Virtual metrology frame

ABSTRACT

This paper presents a method for optimizing the performance of a real-time, long term, and accurate accelerometer based displacement measurement technique, with no physical reference point. The technique was applied in a system for measuring machine frame displacement.

The optimizer has three objectives with the aim to minimize phase delay, gain error and sensor noise. A multi-objective genetic algorithm was used to find Pareto optimal estimator parameters.

The estimator is a combination of a high pass filter and a double integrator. In order to reduce the gain and phase errors two approaches have been used: zero placement and pole-zero placement. These approaches were analysed based on noise measurement at 0g-motion and compared. Only the pole-zero placement approach met the requirements for phase delay, gain error, and sensor noise.

Two validation experiments were carried out with a Pareto optimal estimator. First, long term measurements at 0g-motion with the experimental setup were carried out, which showed displacement error of 27.6 ± 2.3 nm. Second, comparisons between the estimated and laser interferometer displacement measurements of the vibrating frame were conducted. The results showed a discrepancy lower than 2 dB at the required bandwidth.

1. Introduction

In recent decades, many consumer products (e.g., mobile phones and cameras) have seen significant miniaturization, although production machine tools have not seen an equivalent size reduction. A small size machine requires high machine accuracy, high stiffness, and high dynamic performance. The existing solutions to these requirements are antagonistic with small-size constraints. Numerous research efforts to develop small machines have been undertaken over the last two decades [1,2], however, most of these machines are still at the research stage.

The μ4 is a small size CNC machine with 6 axes, which was developed by Cranfield University and Loxham Precision [3]. This machine concept aims at having a high accuracy motion system aligned within a small size constraint.

Machine tool frames have two key functions; 1. Transferring forces and 2. Position reference (metrology frame). There are three main concepts meeting the two required functions [4], which are shown in Fig. 1. In the traditional concept one frame is used for both functions (a). An additional Balance Mass (BM) for compensating servo forces concept (c) [5–7]. Separating the two functions by having an unstressed metrology frame (b) [5,6,8]. Concepts (b) and (c) can be combined to achieve superior performance [4,5].

In a servo system, a force F is applied to achieve the required displacement of the carriage relative to the frame X. A flexible frame will exhibit resonances that are excited by the reaction of the servo-forces. A flexible frame is a significant dynamic effect influencing machine positioning device [4,9,10], especially in the case of small size machine [11]. Fig. 2 shows a 2D model of linear motion system influenced by this dynamic effect.

Realizing concepts other than the Traditional can improve the machine performance; however these concepts are not aligned with a small size requirement. On the other hand, a flexible frame limits the dynamic performance of the small size machine. Thus, a new positioning concept is required.

A novel positioning concept, the *virtual metrology frame*, has been developed [12]. By measuring machine frame vibrational displacement X_f and carriage position relative to the frame X, and fusing both signals, an unperturbed position signal X_{mf} is obtained. Thus, the flexible frame resonances in the plant were attenuated resulting in an improved servo bandwidth of up to 40% [12]. The

* Corresponding author.
E-mail addresses: j.h.abir@cranfield.ac.uk (J. Abir), s.longo@cranfield.ac.uk (S. Longo), P.Morantz@cranfield.ac.uk (P. Morantz), paul.shore@npl.co.uk (P. Shore).

http://dx.doi.org/10.1016/j.mechatronics.2016.07.003
0957-4158/

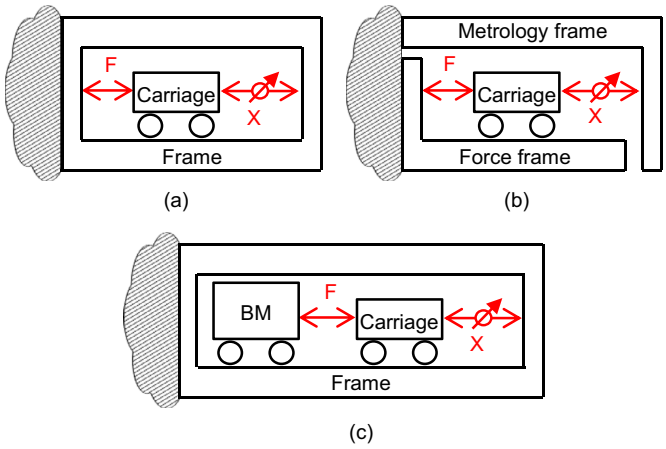

Fig. 1. Three machine frame concepts. Traditional concept (a), two frames concept (b), and additional balance mass concept (c).

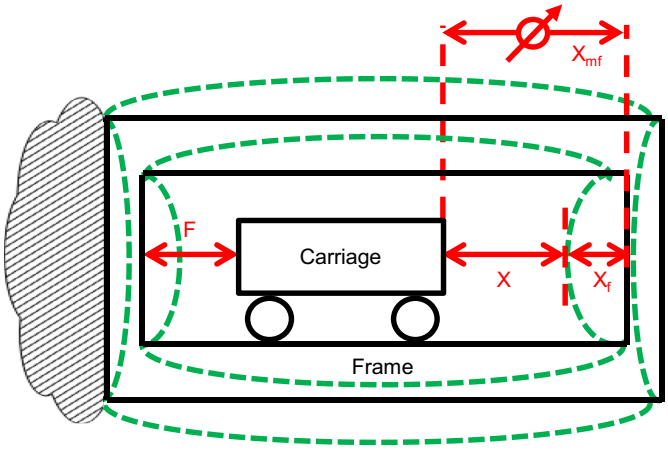

Fig. 2. Motion system 2D model of a flexible frame.

improved machine performance is as if the machine has a physical metrology frame. This novel concept does not require the physical components of a conventional metrology frame; however, realizing this concept requires a technique for real-time measurement of the frame displacement due to vibration.

There are three significant constraints and requirements for measuring the frame vibrational displacement. First, a fixed reference point for measurement is not practical, since having a second machine frame is hard to realize due to the small size constraint. Second, noise characteristics should be comparable to the position sensor noise, e.g., linear encoder. Third, the measurement delays due to signal processing should be smaller than the servo controller update rate.

There are various technologies for precision displacement sensors such as capacitive, eddy current, and inductive sensors [13–15]; however, implementing these sensors requires a fixed reference point.

Strain sensors do not require fixed reference point, and are used for position control due to their simplicity and low cost [13]; however, their main drawback is that they require deformation of the measured component. Vibrational displacement is not necessarily a deformation at the point of measurement, and the deformation can be due to a remote compliance. Hence, the location of mounting the strain sensor is determined by the measured mode shape and its compliance, and not on the point of interest. Furthermore, there are only partially compensating techniques for temperature dependence of strain measurements and long term stability [13]. Thus, strain sensors are not suitable for this purpose.

An accelerometer sensor offers a potentially superior solution as it measures the linear acceleration of a point without a fixed reference system [15]. By double integration, displacement can be obtained directly from the acceleration a:

$$d(t) = \int_0^t \int_0^t a(t)dt^2 + \dot{d}(0) \cdot t + d(0), \tag{1}$$

where $\dot{d}(0)$ and $d(0)$ are the initial velocity and position, respectively. Hence, acceleration based displacement measurement offers an unlimited full-scale-range, as opposed to more common precision displacement technologies [13]. Using accelerometer sensors, frame displacement can be estimated relative to the "unstressed" state, when the frame was static; however, real time, low noise, and low delay acceleration based displacement measurements have not been reported.

Currently, there are a limited number of real-time implementations of displacement measurements based on integration in a control system [16]. This is due to the requirement for small phase delay; and filtering techniques for reducing phase delay can cause gain errors. High accuracy is feasible only for short duration measurements of a narrow bandwidth motion [17] by implementing bandpass filtering techniques. Bandpass filtering reduces the sensor noise outside the required bandwidth, but also causes phase delays.

The standard deviation σ of acceleration based displacement measurements increases as εt^{α}, where t is the integration time, ε represents the accelerometer error, and α is in the range of 1–2 [18,19]. Hence, long term integration (i.e. >10 s) of acceleration signals has been largely unsuccessful [16,17,20]. It has been shown to be achievable under specific conditions e.g., integration in the continuous domain [21], and a narrow bandwidth [22]. The over increasing standard deviation of acceleration based displacement sets a challenge implementing it as a displacement sensor in a machine, which it typical operation time is long term ($>>10$ s).

In this paper, an optimization technique was used to solve the apparently antagonistic requirements for long term (>10 s), real time, and high accuracy (<30 nm) acceleration based displacement measurements. By constraining the measurements to only dynamic displacements, which occur at the flexible frame resonances, a Pareto optimal solution was found.

In Section 2, we present the problem formulation by describing the experimental setup, and the optimization problem. In Section 3, we present displacement estimation noise analysis of the system under test. In Section 4 the estimator design, using a heave filter, is presented. In Section 5, we present the estimator design, and the optimization constraints and goals. In Section 6, the results of the optimization process are presented for zero placement and pole-zero placement filters. In Section 7, optimal estimator performance was validated by comparing the displacement with laser interferometer measurements. We conclude the paper in Section 8.

2. Problem formulation

In this section we describe the experimental setup; a simplified motion module with flexible frame and measurement equipment, and the optimization problem which was solved in this research.

2.1. Experimental setup

A simplified linear motion module, which represents one of the machine motion modules [23], consists of: air-bearings, frame, linear motor, linear encoder, and carriage. (Fig. 3); the motion module frame was fixed to a vibration isolation table.

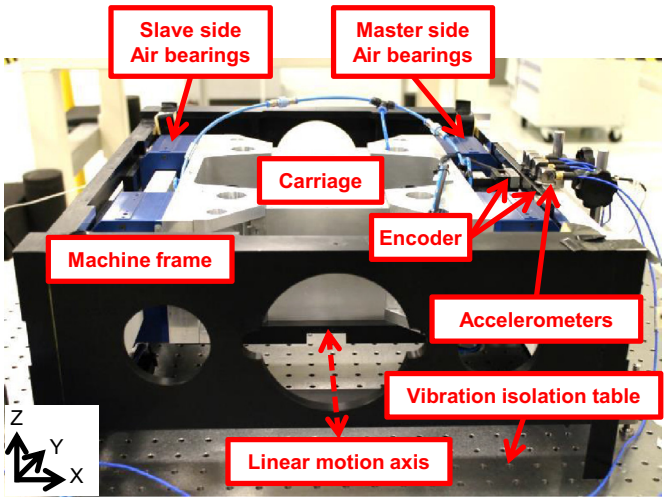

Fig. 3. A simplified linear motion module.

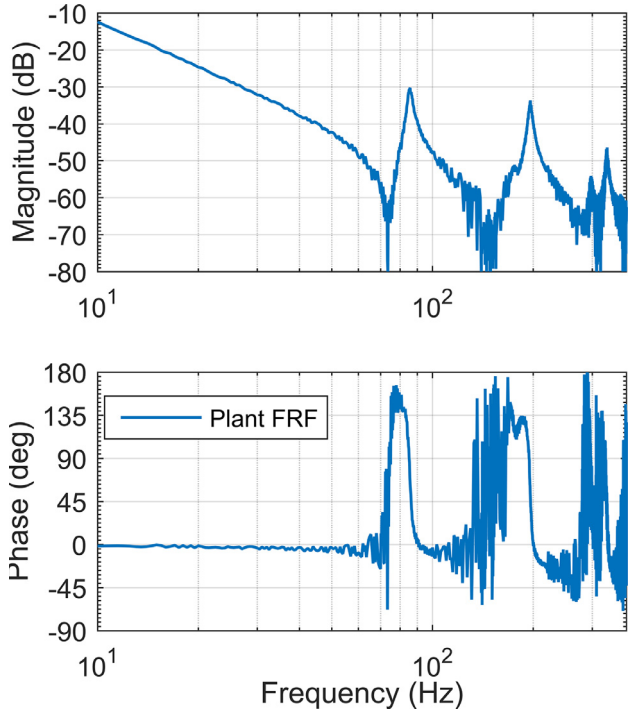

Fig. 4. Plant Frequency Response Function (FRF).

The driving force and the sensor are not applied at the center of gravity, but on the "master side". Thus, the carriage movement relies on the high stiffness of the guiding system, which suppresses motion in an undesired direction.

The plant Frequency Response Function (FRF) (Fig. 4) was measured from the input force F to the position measurement X. The input force was a swept sine signal, with frequency 5–500 Hz, which was generated as current command by the linear motion controller; this enabled analysis of the system mechanical resonances effects.

The plant FRF shows characteristics of type Antiresonance–Resonance (AR), which corresponds to flexible frame and guiding system flexibility [9,24]. Thus, Finite Element Analysis (FEA) and Experimental Modal Analysis (EMA) techniques have been used [11,25], which showed a flexible frame phenomena. Fig. 5 shows a flexible frame mode shape measured using EMA. The frame flexible mode (b) is measured by the encoder due to the relative movement between the frame and the carriage, which appears as resonance in the plant FRF (Fig. 4). This is because the encoder scale is mounted to the machine frame, while its read-head is mounted to the carriage (Fig. 6).

Low noise Integrated Electronics PiezoElectric (IEPE) accelerometers are the appropriate sensors for small vibration signals measurements due to their: low noise; wide dynamic, frequency, and temperature range; high sensitivity; and small size [26]. Triaxial ceramic shear accelerometers (PCB 356A025) were used for the EMA and measuring the frame displacement (Fig. 3). The accelerometer sensitivity is 25 mV/g, the measurement range is ± 200 g peak, and the frequency range is 1–5000 Hz. The simplified motion module was fixed to a vibration isolation table to suppress any ground vibrations that may introduce extra noise in the measurements (Fig. 3).

A signal conditioner is required to power the IEPE accelerometer with a constant current, and to decouple the acceleration signal. A low noise analog gain switching signal conditioner was used (PCB 482C15).

Digital Signal Processing (DSP) was performed using a real-time target machine (Speedgoat performance real-time target machine). It contains 16 I/O channels and 16 bit Analog to Digital Converter (ADC). The conversion time for each ADC is 5 µs. The target machine is optimized for MathWorks® SIMULINK® and xPC Target™.

The frame displacement x_f was estimated by measuring frame vibration a_f using low noise accelerometers; the signal was acquired by the ADC and passed through the estimator. It is composed of a High Pass Filter (HPF) to reduce low frequency noise and a numerical double integrator (Fig. 7).

Laser interferometer (Renishaw ML10 Gold Standard) was used to validate the estimated displacement. The laser light is split into two paths by a beam splitter, one that is reflected by a "dynamic" retroreflector and another reflected by a "stationary" retroreflector (Fig. 8a). The dynamic retroreflector was mounted to the machine frame, and an accelerometer mounted to the retroreflector (Fig. 8b). The stationery retroreflector was fixed using an optics holder. Note that this validation setup can only be realized on the simplified motion system, and not on the full machine. The displacement of the dynamic retroreflector is measured by counting the number of interference events. The interferometer can measure dynamic displacement at a sampling rate of 5000 Hz with a resolution of 1 nm.

2.2. The optimization problem

Real-time implementation of displacement measurements based on integration in a control system requires small phase delay, low gain error, and high sensor noise removal. The multi-objective optimization problem can be formally defined as: find the vector $\vec{x} = [\vec{x}_1, \vec{x}_2, \ldots, \vec{x}_n]^T$, which satisfies n constrains (2)

$$g_i\left(\vec{x}\right) \geq 0\,,\ i = 1, \ldots, n, \tag{2}$$

and optimize the vector function

$$\vec{J}(\vec{x}) = [\vec{J}_\sigma(\vec{x}), \vec{J}_{Mag}(\vec{x}), \vec{J}_{Phase}(\vec{x})]^T, \tag{3}$$

where $\vec{x}$ is the estimator parameters vector that simultaneously minimizes the three error functions: noise error function J_σ, magnitude error function J_{Mag}, and phase error function J_{Phase}.

3. Displacement estimation noise analysis

This section presents the noise sources in the acceleration measurement, and the effect of acceleration noise on the displacement estimation.

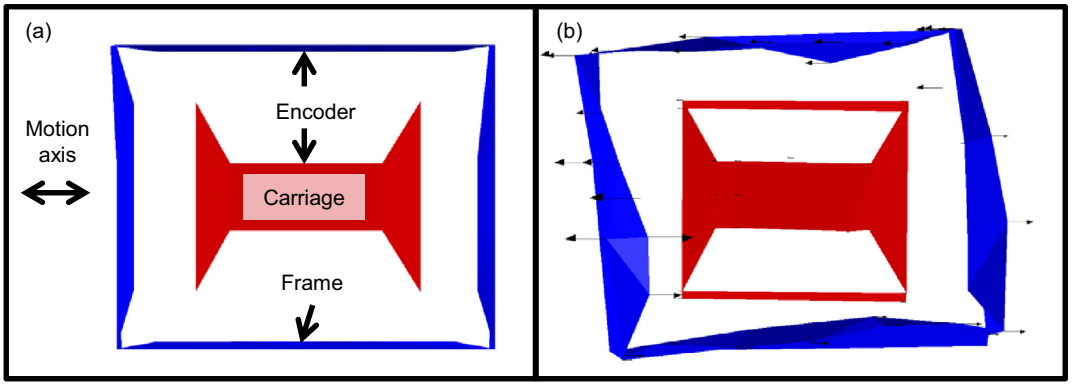

Fig. 5. Experimental modal analysis results. Unstressed frame (a), and a flexible frame mode shape at 305 Hz (b). The length of the arrows in (b) represents the mode shape magnitude.

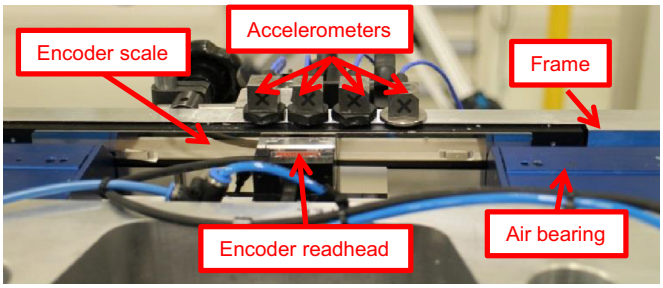

Fig. 6. Setup of four IEPE accelerometers mounted to the machine frame.

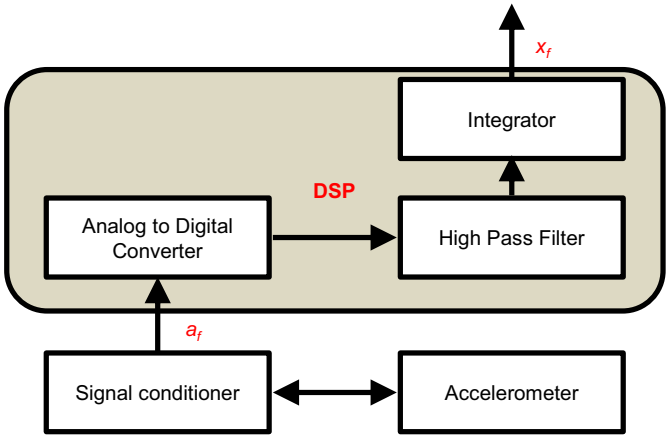

Fig. 7. Estimating displacement x_f by acceleration signal a_f block diagram.

There are three uncorrelated sources that contribute to the displacement measurement noise (Fig. 9): accelerometer, signal conditioner and ADC. The Power Spectral Density (PSD) of each source is usually specified by the manufacturer. The accelerometer has the lowest noise contribution; however, to improve the Signal to Noise Ratio (SNR) a x100 gain is used. Thus, the accelerometer noise is the most significant noise source.

It is difficult to interpret the noise contribution of a specific bandwidth from a PSD graph, which can be circumvented by calculating the Cumulative Power Spectrum (CPS) [27]:

$$CPS(f) = \int_{f_s}^{f_e} PSD(\upsilon)/(2\pi \cdot \upsilon)^4 d\upsilon. \tag{4}$$

Note that the sensor PSD is in acceleration units and the CPS is in displacement, thus the PSD is multiplied by $(2\pi \cdot f)^{-4}$. The CPS graph (Fig. 10) shows that the expected displacement noise is $\sim 10\,\mu m$ mainly due to low frequency noise < 5 Hz; however, this is an optimistic analysis since it was not considered low frequency noise (<1 Hz).

In [17,28] an empirical formula was suggested for resolution estimation of the displacement measurement $\bar{A}$ based on the accelerometer spectral density ρ and measurement time T_m:

$$\bar{A}(\rho, T_m) = \eta \left(\int_{(1-\nu)/T_m}^{(1+\nu)/T_m} \rho(f) df \right)^{0.5} T_m^2, \tag{5}$$

where ν is experimentally determined constant, and η depending upon signal acquisition and conditioning [29]. The displacement noise resembles a sine wave, whose frequency is close to $T_m{}^{-1}$, and its amplitude is $\bar{A}$.

Eq. (5) can be transformed to estimate the maximum allowance low-frequency noise ρ_{LF} for a given resolution $\bar{A}$ and measurement time T_m:

$$\rho_{LF} = \frac{\left(2\pi^2 \cdot \bar{A}\right)^2}{\nu \cdot T_m^3}. \tag{6}$$

For example, to achieve the resolution of $\bar{A} = 30$ nm for duration of $T_m = 20$ s the low frequency noise should be $\rho_{LF} \le 1.75 \cdot 10^{-4} (\mu m/s^2)^2/Hz$. This low noise requirement is technologically feasible [26,30–32], but there is no information at very low frequencies required for long duration measurements [28].

Based on the noise analysis, the displacement estimator must reduce the low frequency noise significantly as there are at least ten orders of magnitude difference between the required and expected noise level. By plotting the CPS (4) as a function of f_s one can assess the minimum required cut-off frequency for an HPF (Fig. 11). By finding the intersection of the CPS line with the required noise level, 30 nm, the minimum cut-off frequency was found to be 17 Hz.

4. Estimator design

This section presents an estimator design based on a combination of a high pass filter and a double integrator, and phase correction techniques.

An accelerometer can be regarded as a single-degree-of-freedom mechanical system, with a simple mass, spring, and damper [33]. Its output signal can be represented as [34]:

$$a(t) = k_a \ddot{x}(t) + w(t) + w_0, \tag{7}$$

where k_a is the accelerometer gain, $\ddot{x}$ is the acceleration acting on the accelerometer, $w(t)$ is the noise and disturbance effect, and w_0 is the 0g-offset.

Although integration is the most direct method to obtain displacement from acceleration, due to 0g-offset and low frequency

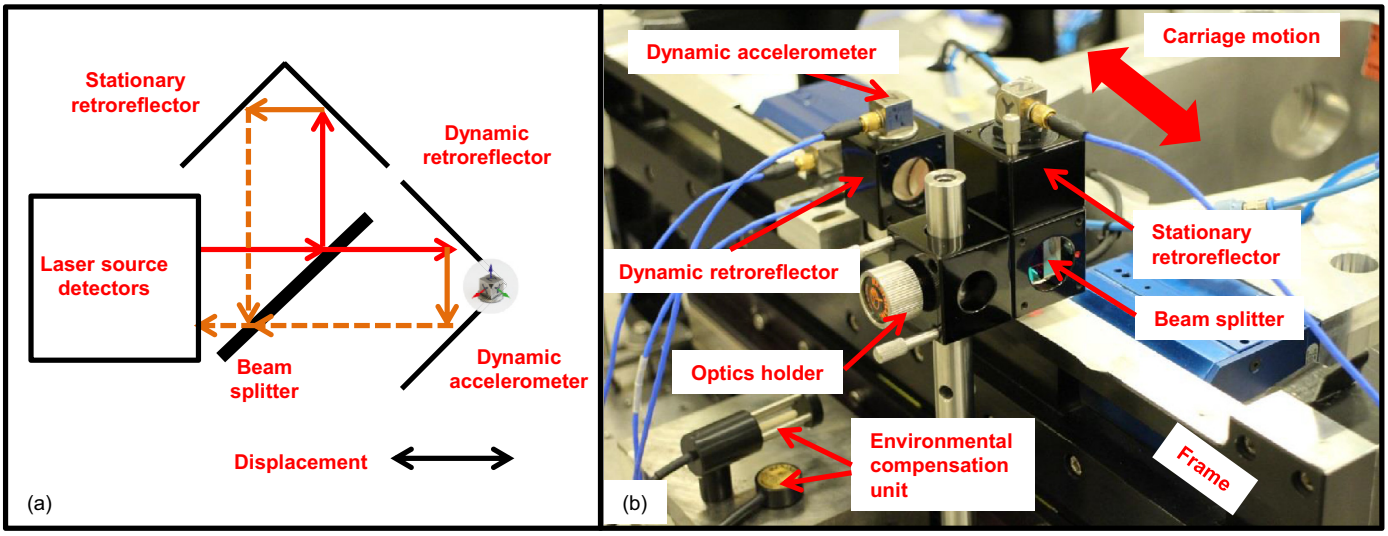

Fig. 8. Setup of the displacement validation experiment.

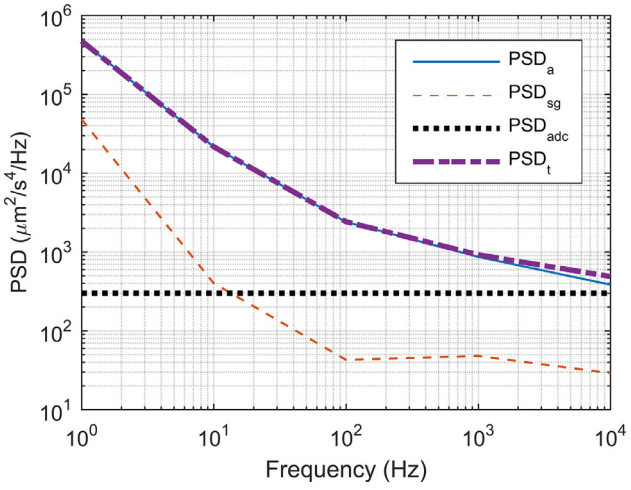

Fig. 9. Power Spectral Density of accelerometer multiplied by 100x gain PSD_a, signal conditioner PSD_{sg}, ADC PSD_{adc} and the total Power Spectral Density PSD_t.

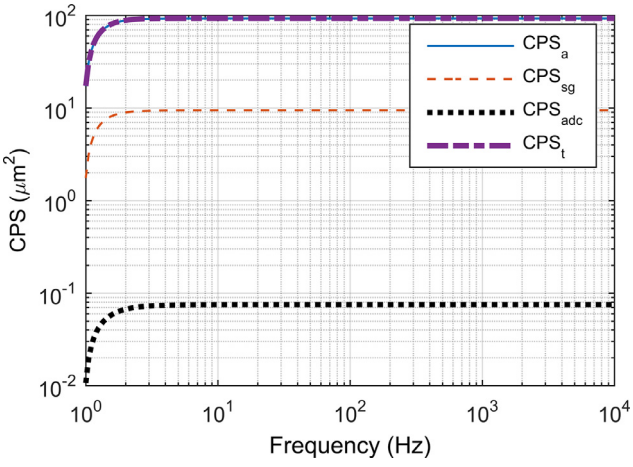

Fig. 10. Cumulative Power Spectrum of accelerometer multiplied by 100x gain, signal conditioner, ADC, and total Cumulative Power Spectrum, CPS_a, CPS_{sg}, CPS_{adc}, and CPS_t respectively. $f_s = 1$ Hz as PSD is not specified for lower frequencies.

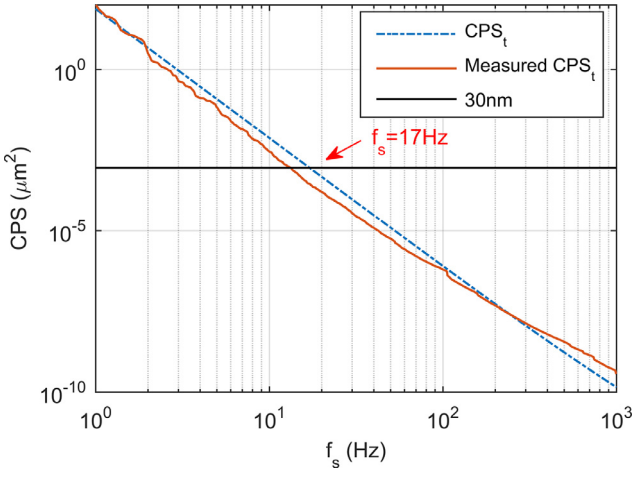

Fig. 11. CPS as a function of f_s.

noise it is not appropriate to integrate the acceleration signal directly. The integration process leads to an output that has a Root Mean Square (RMS) value that increases with integration time [20]. This can be a problem even in the absence of any motion of the accelerometer, due to the 0g-offset [18,35]. Displacement estimation based on digital integration was shown to have lower noise compared to analog integration. Furthermore, at high sampling rates the digital integration showed higher accuracy [16].

Numerical integrators can be used in the time domain [20,36,37] and in the frequency domain [15,38]; however, using frequency domain techniques for real time application is difficult, as it suffers from severe discretization errors, if the discrete Fourier transform is performed on a relatively short time interval [15,39]. Hence, the digital estimator will be in the time domain.

A HPF is used to remove constant or low frequency offsets (0g-offset) and to reduce the low frequency noise. Without it, the double integrated signal will diverge due to the double integration behavior. Tuning the HPF, an optimized cut-off frequency, ω_c, takes into consideration good tracking of the actual displacement, removal of sensor noise and offsets, and low phase errors [40]. Reduced gain and phase lead error are associated with a high cut-off frequency, whereas high noise gain is associated with a low cut-off frequency.

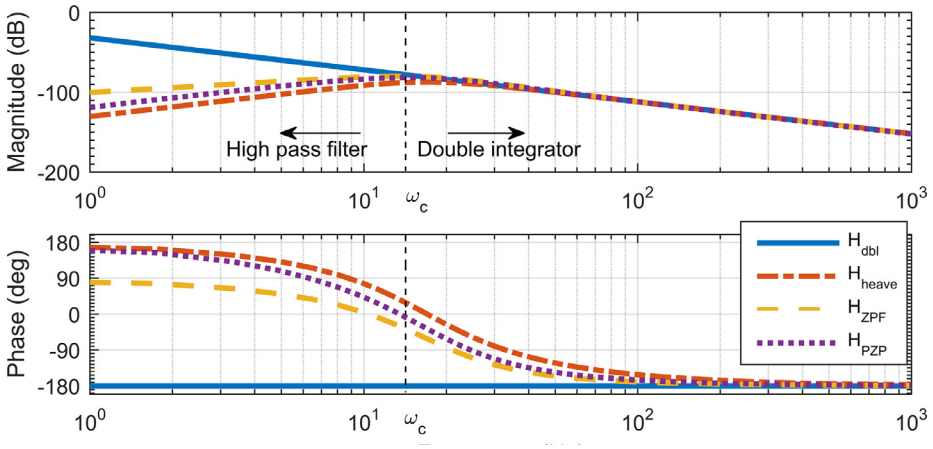

Fig. 12. Comparison of heave filters and ideal double integrator Bode plots. H_{dbl} is an ideal double integrator. H_{heave}, H_{ZPF}, and H_{PZP} are the heave filter, heave filter with zero-placement filter, and heave filter with pole-zero-placement filter respectively, where $\omega_c = 17$ Hz and $\varsigma = 1/\sqrt{2}$.

An estimator based on a combination of an HPF and a double integrator (heave filter) is given by [40]:

$$H_{heave} = \frac{\hat{D}}{a}(s) = \frac{s^2}{(s^2 + 2\varsigma\omega_c + {\omega_c}^2)^2}, \tag{8}$$

where s is the Laplace variable, ς the damping coefficient, and ω_c the cut-off frequency of the filter. The displacement estimate is denoted by $\hat{D}$. Usually $\varsigma=1/\sqrt{2}$, to obtain a Butterworth contour. It was used for estimating the heave position of a ship due to sea waves [40,41], and displacement of optical elements due to structural vibrations [22] using accelerometer. The drawback of the heave filter is phase errors, which can be reduced by using an All Pass Filter (APF), Zero Placement Filter (ZPF) or Pole-Zero Placement (PZP).

The APF can eliminate the phase error for one specific frequency thus it is not applicable for our case. In ZPF (9), one of the zeros z_a is placed to reduce significantly the phase error; however, it attenuates noise less at low frequencies [41]. In PZP (10), a pole p and zero z are added to the heave filter with an additional gain parameter K.

$$H_{ZPF} = \frac{s(s + z_a)}{(s^2 + 2\varsigma\omega_c + {\omega_c}^2)^2} \tag{9}$$

$$H_{PZP} = \frac{s^2}{(s^2 + 2\varsigma\omega_c + {\omega_c}^2)^2} \cdot K\frac{s - z}{s - p} \tag{10}$$

In Fig. 12 a comparison of heave filters with phase correction filter and ideal double integrator (11) is shown, where the minimum cut-off frequency $\omega_c = 17$ Hz was based on the displacement noise analysis (Fig. 11). As can be seen, the filters magnitude above the cut-off frequency is as a double integrator; however, the phase differs significantly from the ideal -180^o phase even for frequencies $> 3\cdot\omega_c$.

$$H_{dbl} = \frac{\hat{D}}{a}(s) = \frac{1}{s^2} \tag{11}$$

5. Optimizer design

This section describes the optimizer design, its constraints and goals, and the three error functions. The design is independent of the estimator design.

During the last decade, it was shown that evolutionary algorithms are useful in solving multi-objective optimization problems. There are various techniques which can be used, however the Genetic Algorithm (GA) approach was chosen. It has been shown that GA is suitable for solving complex mechatronics problems [42–44] especially for signal processing [45], and for multi-objectives problems [46,47].

As there are three objectives (J_σ, J_{Phase}, J_{Mag}) a Multi-Objective Genetic Algorithm (MOGA) optimizer was chosen using Matlab global optimization toolbox [48]. The algorithm scans the whole search domain and exploits promising areas by selection, crossover and mutation applied to individuals in population. In multi-objective optimization, the aim is to find good compromises rather than a single solution. An optimal solution $\vec{x}^*$ is found if there exists no feasible $\vec{x}$ which would decrease one objective without causing a simultaneous increase in at least one other objective. The image of the optimal solutions is called the "Pareto Front". The decision maker chooses a solution from the Pareto optimal solutions which compromise and satisfies the objectives as possible. A detailed explanation of the GA process can be found in [45–47,49]. For three objective functions it gives a surface in three-dimensional space. Thus, the "optimal" solution is chosen by the designer.

The vector $\vec{x}$ is defined by the estimator parameters in the cases of ZPF (12) and PZP (13). To obtain a Butterworth contour $\varsigma=1/\sqrt{2}$.

$$\vec{x} = [\vec{\omega}_c, \vec{z}_a]^T \tag{12}$$

$$\vec{x} = [\vec{\omega}_c, \vec{K}, \vec{z}, \vec{p}]^T \tag{13}$$

5.1. Error functions

As described in Section 2, there are three displacement estimation error functions: noise error function J_σ, magnitude error function J_{Mag}, and phase error function J_{Phase}.

The noise error function is defined as the RMS value $\sigma_{\hat{D}}$ of the displacement signal generated by the estimator:

$$J_\sigma \cdot T_\sigma = \sigma_{\hat{D}}, \tag{14}$$

where T_σ is noise normalization factor.

In section 3 it was shown that low frequency acceleration noise is the main contributor to J_σ, however usually there is no specification for noise at these frequencies. Hence, for this calculation a "0g-motion" acceleration noise measurements were used. A typical 0g-motion acceleration signal was measured at a sampling rate of 32 kHz for $t = 20$ s. The measured CPS and the expected CPS are in good agreement as can be seen in Fig. 11.

The magnitude and phase error functions are defined as the difference between the magnitude and phase response of the estimator and an ideal double integrator. The magnitude error function

is:

$$J_{Mag} \cdot T_{Mag} = \sum_{i=1}^{n} |M_{dbl}(f_i) - M_{HF}(f_i)| \cdot w_i, \tag{15}$$

where $M_{dbl}(f_i)$ and $M_{HF}(f_i)$ are the magnitude response of an ideal double integrator and the estimator at frequency f_i, respectively, w_i is a weighting vector, and T_{Mag} is the magnitude normalization factor. The phase error function is:

$$J_{Phase} \cdot T_{Phase} = \sum_{i=1}^{n} |P_{dbl}(f_i) - P_{HF}(f_i)| \cdot w_i, \tag{16}$$

where $P_{dbl}(f_i)$ and $P_{HF}(f_i)$ are the phase response of the ideal double integrator and the estimator at frequency f_i, respectively. T_{Phase} is the phase normalization factor.

For simplicity the frequencies f_i, that were used to calculate the error functions, are the frame resonances which are obtained from the plant FRF (Fig. 4); however, one can use a different frequency vector (and it corresponding weighing vector w_i).

5.2. Optimizer constraints and goals

The goals for the noise and phase errors are set due to system requirements. The noise level is required to be comparable to the linear encoder noise (17), and the phase error is required to be smaller than the servo control update rate (18). The magnitude error was set empirically (19).

$$J_\sigma < 30\text{nm} \tag{17}$$

$$J_{Phase} < 70\mu\text{s} \tag{18}$$

$$J_{Mag} < 3\text{dB} \tag{19}$$

The maximum constraint to the cut-off frequency ω_c is defined by the first antiresonance frequency (Fig. 4), as above that frequency frame vibrational displacement occurs. The minimum constraint to the cut-off frequency was calculated in Section 3 using the CPS plot (Fig. 10). Hence, the constraints for the cut-off frequency are

$$17 \cdot 2\pi \text{ rad/s} \le \omega_c \le 75 \cdot 2\pi \text{ rad/s}. \tag{20}$$

In the case of ZPF, the maximum constraint for the zero placement z_a is given [40]. The minimum constraint is that it has no zero placement hence,

$$0 < z_a \le 2\sqrt{2} \cdot \omega_c = 1332.9 \text{ rad/s}. \tag{21}$$

In the case of PZP, the gain factor K has the constraints of

$$0 < K \le 1. \tag{22}$$

There is no analytical equation for the pole and zero values; however, one should consider a stable filter where

$$\frac{z}{p} > 1. \tag{23}$$

Thus, an empirical approach was used to set the pole and zero constraints:

$$-3000 \le z, p < 0. \tag{24}$$

6. Results of the optimization process

This section presents the optimization results and its Pareto front graphs for the two estimator designs ZPF and PZP.

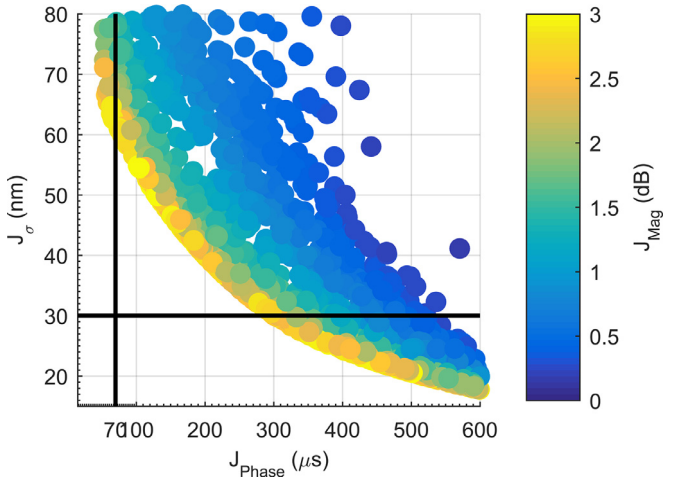

Fig. 13. Pareto front of H_{ZPF} when $\varsigma = 1/\sqrt{2}$.

6.1. Zero placement filter

The Pareto front graph of the ZPF estimator with Butterworth contour is shown in Fig. 13. The main conflicting objectives are the phase error and noise level. No optimal solution which meets the optimization goals (17–19) was found. Allowing an underdamped estimator, where $0 < \varsigma \le 1/\sqrt{2}$, improves the phase response at the expense of having a resonant peak. Hence, a higher cut-off frequency is possible which reduces the sensor noise and phase error; however, no optimal solution which meets all three requirements was found.

Thus, a ZPF estimator design with either Butterworth contour or underdamp properties is not an appropriate solution for the problem.

A new approach was proposed by splitting the denominator into two different filters, which adds two degrees of freedom to the ZPF design (25).

$$\tilde{H}_{ZPF} = \frac{s \cdot (s + z_a)}{\left(s^2 + 2\varsigma_1\omega_{c1} + {\omega_{c1}}^2\right) \cdot \left(s^2 + 2\varsigma_2\omega_{c2} + {\omega_{c2}}^2\right)} \tag{25}$$

Hence, its new parameters vector is $\vec{x} = [\vec{\omega}_{c1}, \vec{\omega}_{c2}, \vec{\varsigma}_1, \vec{\varsigma}_2, \vec{z}_a]^T$. This new approach shows improvement of the Pareto front results however, no results were found which meets the requirements.

6.2. Pole-zero placement filter

The Pareto front graph of the PZP estimator with Butterworth contour is shown in Fig. 14. Again in this case there is no solution which meets the requirements, although it shows better results compared to Fig. 13.

Allowing an underdamped estimator, where $0 < \varsigma \le 1/\sqrt{2}$ gives an optimal solutions which meets the set of requirements (Fig. 15). Using the new approach with split denominator:

$$\tilde{H}_{PZP} = \frac{s^2}{(s^2 + 2\varsigma_1\omega_{c1} + {\omega_{c1}}^2) \cdot (s^2 + 2\varsigma_2\omega_{c2} + {\omega_{c2}}^2)} \cdot K\frac{s - z}{s - p}, \tag{26}$$

and parameter vector $\vec{x} = [\vec{\omega}_{c1}, \vec{\omega}_{c2}, \vec{\varsigma}_1, \vec{\varsigma}_2, \vec{K}, \vec{z}, \vec{p}]^T$, shows similar results. Thus, based on Fig. 15 an optimized estimator was chosen with the following parameters: $\varsigma = 0.37$, $\omega_c = 214.82$ rad/s, $K = 0.69$, $z = -429.29$, $p = -11.90$.

Comparing the Butterworth contour and underdamped H_{PZP} transfer functions (Fig. 16) emphasizes that a lower damping ratio allows higher cut-off frequency at the expense of a resonant peak.

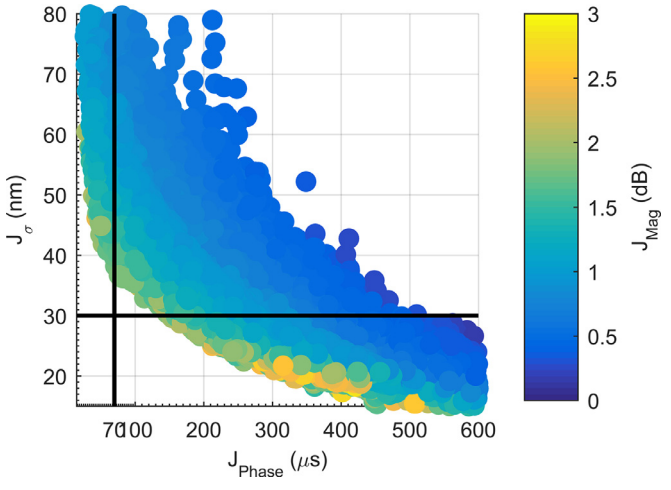

Fig. 14. Pareto front of H_{PZP} when $\varsigma = 1/\sqrt{2}$.

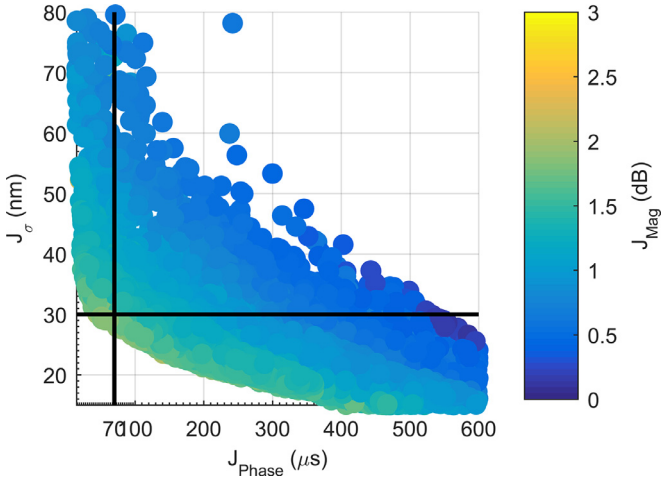

Fig. 15. Pareto front of H_{PZP} when $0 < \varsigma \leq 1/\sqrt{2}$.

Above the cut-off frequency the ZPF design has a positive gain error, while in PZP designs it changes its sign. Moreover, a significant difference in the low frequency noise reduction between the ZPF and PZP designs can be observed. The PZP designs have a better noise reduction.

7. Estimator validation

This section shows the experimental results validating an optimal PZP estimator design. There are three main experiments for validating the estimator performance: (i) robustness of the design; (ii) long term measurements at 0g-motion; and (iii) a comparison of displacement signals due to structural vibrations between laser interferometer sensor and the displacement based acceleration.

7.1. 0g-motion noise and robustness validation

Using the optimized estimator, 0g-motion measurement was made with four tri-axial accelerometers (12 accelerometers) as shown in Fig. 6. The setup is detailed in Section 2.1. The signals were acquired at a sampling rate of 54 kHz for $t = 600$ s. The achieved displacement RMS is 27.6 ± 2.3 nm. Furthermore, the low variance between all of the accelerometers assures that the estimator design is robust, and not accelerometer dependent. Fig. 17a shows the estimated displacement of 0g-motion measurement, i.e. the RMS noise, of one typical accelerometer. The results are in agreement with the requirements (17). Fig. 17b shows the changes in displacement noise RMS over measurement time. As required from the estimator, 0g-offset and low frequency noise are attenuated which allows long term double integration without diverging.

7.2. Displacement estimation validation

The validation was made by comparing the displacement measured by the laser interferometer and the acceleration based displacement measurement of the machine frame vibrations. The frame was excited using an oscillating position command generated by the linear motion controller, $X_{set} = A_i \cdot \sin(\omega_i t)$, at various frequencies ω_i and amplitudes A_i (Table 1). Note that A_i is the commanded carriage movement amplitude; hence the frame exhibits different displacement due to the servo reaction forces. The frame displacement amplitudes measured by the laser interferometer ($A_{L,i}$) and acceleration based displacement ($A_{est,i}$) were extracted using a Fast Fourier Transform (FFT). The discrepancy between the measurements meets the specified requirements (19). Fig. 18 shows an example of the discrepancy in the measured frame displacement at 100 Hz.

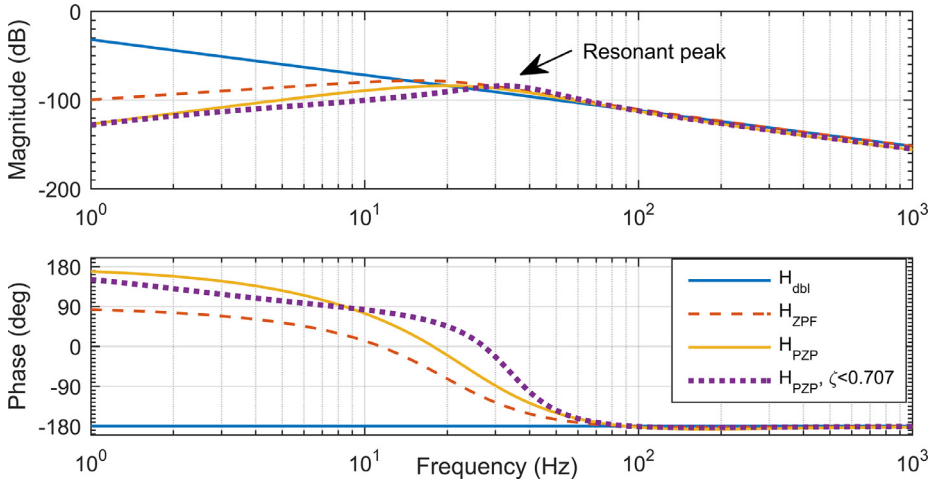

Fig. 16. Comparison of optimized heave filters and the ideal double integrator. H_{dbl} is an ideal double integrator. H_{ZPF} and H_{PZP} are optimized heave filters with zero-placement filter and with pole-zero-placement filter respectively.

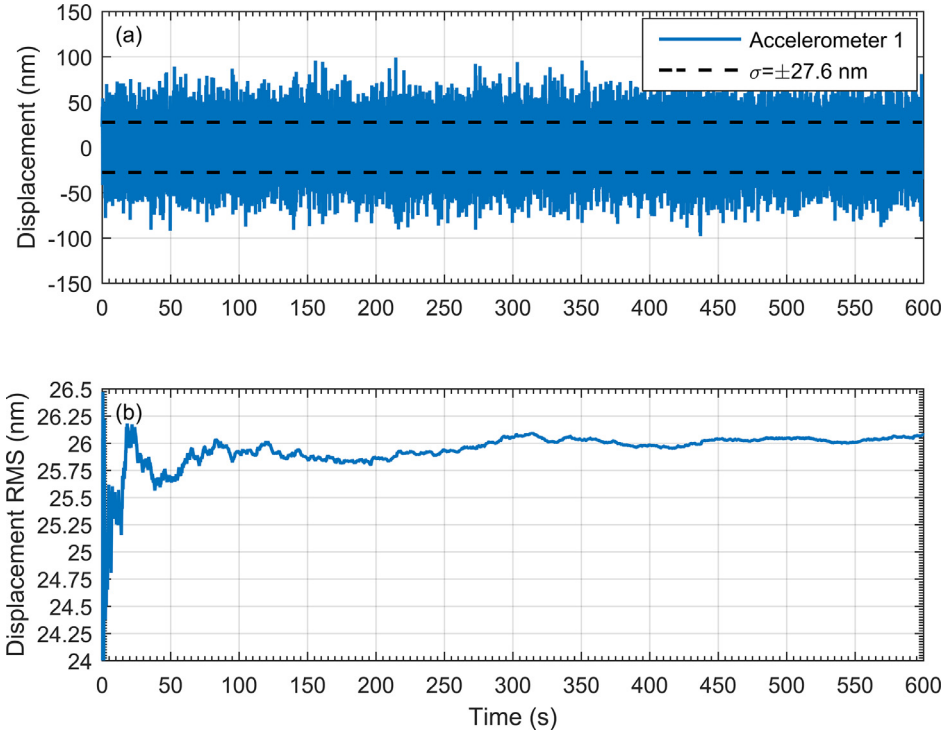

Fig. 17. Displacement estimation noise measurement. (a) Noise in long term measurement for $t = 600$ s. (b) Noise Root Mean Square (RMS) of the displacement signal.

Table 1
Results of displacement estiamtion validation.

i	ω_i [Hz]	A_i [nm]	$A_{L,i}$ [nm]	$A_{est,i}$ [nm]	Discrepancy [dB]
1	80	40,000	1533.0	1932.0	2.0
2	100	15,000	741.0	751.0	0.1
3	100	20,000	981.6	998.9	0.1
4	120	14,000	292.4	261.2	0.9
5	150	20,000	263.2	232.2	1.0
6	200	20,000	93.5	78.6	1.5

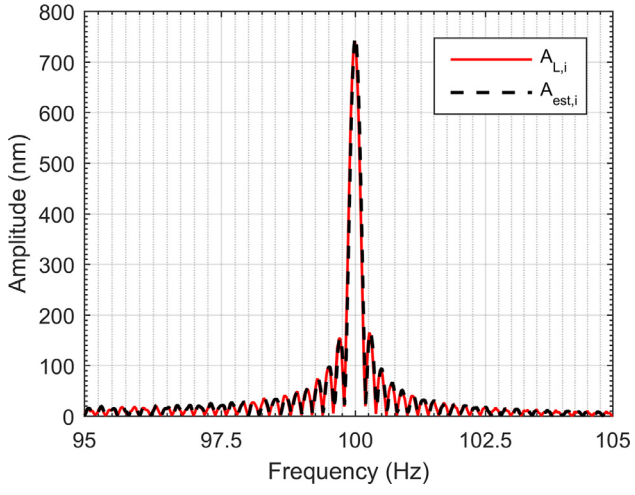

Fig. 18. Displacement estimation validation at $X_{set} = 15{,}000 \cdot \sin(100 \cdot 2\pi \cdot t)$. $A_{L,i}$ and $A_{est,i}$ are the frame displacement amplitude measured by the laser interferometer and acceleration based displacement respectively.

8. Conclusions

This research shows that accelerometers can be used to measure real-time displacement in the nanometer range without constraints to the integration time.

Common displacement sensors require a reference point, which does not always exist. Thus, the novelty of this technique is the ability to measure the dynamic displacement of a structure without having a physical reference point, but instead using a “virtual” reference point. Doing so, it was assumed that the initial conditions of the frame is unstressed state and in rest. The feasibility of this technique depends on the lowest frequency required to be measure since that low frequency noise is the most significant cause of displacement error. Although the displacement noise and measurement bandwidth met the requirements, by using an accelerometer with higher performance the displacement noise can be reduced significantly and the measurement bandwidth can be extended towards 0 Hz. Furthermore, using acceleration based dynamic displacement measurement technique offers an unlimited full-scale-range sensor in the nanometer range.

The optimized estimator showed less than 10% variation in the displacement noise with different accelerometers (from the same model) which demonstrate its robustness.

The developed technique is essential to realize the virtual metrology frame concept. Thus, it was implemented in a machine with a flexible frame improved it dynamic performance.

Acknowledgement

This work was supported by the UK EPSRC under grant EP/I033491/1 and the Centre for Innovative Manufacturing in Ultra-Precision. The author is grateful to the McKeown Precision Engineering and Nanotechnology foundation at Cranfield University, and B’nai B’rith Leo Baeck (London) for their financial support.

References

[1] Huo D, Cheng K, Wardle F. Int J Adv Manuf Technol 2010;47:867–77.
[2] Brecher C, Utsch P, Klar R, Wenzel C. Int J Mach Tools Manuf 2010;50:328–34.
[3] Shore P, Morantz P, Read R. 10th Int. conf. exhib. laser metrol. mach. tool, c. robot. performance., euspen; 2013.
[4] H Soemers, Design principles: for precision mechanisms, T-Pointprint, 2011.
[5] Butler H. IEEE Control Syst Mag 2011;31:28–47.
[6] Fan KC, Fei YT, Yu XF, Chen YJ, Wang WL, Chen F, et al. Meas Sci Technol 2006;17:524–32.
[7] Takahashi M, Yoshioka H, Shinno H. J Adv Mech Des Syst Manuf 2008;2:356–65.
[8] Leadbeater PB, Clarke M, Wills-Moren WJ, Wilson TJ. Precis Eng 1989;11:191–6.
[9] Coelingh E, De Vries TJA, Koster R. IEEE/ASME Trans Mechatron 2002;7:269–79.
[10] Rankers AM, van Eijk J. In: Proc. second int. conf. motion vib. control. yokohama; 1994. p. 711–16.
[11] Abir J, Morantz P, Shore P. In: Proc. 15th int. conf. eur. soc. precis. eng. nanotechnol.; 2015. p. 219–20.
[12] Abir J, Morantz P, Longo S, Shore P. In: ASPE 2016 spring top. meet. precis. mechatron. syst. des. control, american society for precision engineering, ASPE; 2016. p. 58–61.
[13] Fleming AJ. Sens Actuators A 2013;190:106–26.
[14] Gao W, Kim SW, Bosse H, Haitjema H, Chen YL, Lu XD, et al. CIRP Ann Manuf Technol 2015;64:773–96.
[15] Ribeiro JGT, De Castro JTP. IMAC-XXI A conf. expo. struct. dyn.; 2003.
[16] Celik O, Gilbert HB, O'Malley MK. In: IEEE/ASME trans. mechatronics, 18; 2013. p. 812–17.
[17] Spiewak SA, Ludwick SJ, Hauer G. J Manuf Sci Eng 2013;135:021015.
[18] Thong YK, Woolfson MS, Crowe JA, Hayes-Gill BR, Challis RE. Meas Sci Technol 2002;13:1163–72.
[19] Farrell J. The global positioning system & inertial navigation. McGraw Hill Professional; 1999.
[20] Thong YK, Woolfson MS, Crowe JA, Hayes-Gill BR, Jones DA. Meas J Int Meas Confed 2004;36:73–92.
[21] Gilbert HB, Celik O, O'Malley MK. In: IEEE/ASME int. conf. adv. intell. mechatronics. AIM; 2010. p. 453–8.
[22] Keck A. In: Int. fed. autom. control world congr.; 2014. p. 7467–73.
[23] Abir J, Shore P, Morantz P. In: Laser metrol. mach. perform. XI - 11th int. conf. exhib. laser metrol. mach. tool, C. robot. performance, LAMDAMAP 2015, euspen; 2015. p. 126–35.
[24] Rankers AM. Machine dynamics in mechatronics Systems, an engineering approach. University of Twente; 1997.
[25] Abir J, Shore P, Morantz P. In: Proc. 12th int. conf. manuf. res. (ICMR 2014); 2014. p. 35–40.
[26] Levinzon FA. IEEE Sens J 2004;4:108–11.
[27] Jabben L, van Eijk J. Mikroniek 2011;51:5–12.
[28] Spiewak S, Zaiss C, Ludwick SJ. In: Proc. ASME 2013 int. mech. eng. congr. expo.. ASME; 2013. p. 77.
[29] Oppenheim AV, Schafer RW. Discretet-ime signal processing. Englewood Cliffs: Prentice Hall Press; 2009.
[30] Krishnamoorthy U, Olsson RH, Bogart GR, Baker MS, Carr DW, Swiler TP, et al. Sensors Actuators A Phys 2008;145–146:283–90.
[31] Merchant BJ. Seism. instrum. technol. symp.; 2009.
[32] Brownjohn JMW. In: Proc. 25th int. modal anal. conf. (IMAC XXV); 2007. p. 1–8.
[33] Levinzon F. Piezoelectric accelerometers with integral electronics. Springer; 2015.
[34] Zhu W-H, Lamarche T. Ind Electron IEEE Trans 2007;54:2706–15.
[35] Thenozhi S, Yu W, Garrido R. Trans Inst Meas Control 2013;35:824–33.
[36] Gavin HP, Morales R, Reilly K. Rev Sci Instrum 1998;69:2171.
[37] Razavi SH, Abolmaali A, Ghassemieh M. Comput Methods Appl Math 2007;7:227–38.
[38] Worden K. Mech Syst Signal Process 1990;4:295–319.
[39] Lee HS, Hong YH, Park HW. Int J Numer Methods Eng 2011;82:1885–91.
[40] Godhaven J-M. In: IEEE ocean. eng. soc. ocean. conf. proc.. IEEE; 1998. p. 174–8.
[41] Richter M, Schneider K, Walser D, Sawodny O. In: Int. fed. autom. control world congr.; 2014. p. 10119–25.
[42] Lin C-L, Jan H-YJ, Shieh N-C. IEEE/ASME Trans Mechatron 2003;8:56–65.
[43] Ito K, Iwasaki M, Matsui N. IEEE/ASME Trans Mechatron 2001;6:143–8.
[44] Van Brussel H, Sas P, Németh I, De Fonseca P, Van Den Braembussche P. IEEE/ASME Trans Mechatron 2001;6:90–105.
[45] Tang KS, Man KF, Kwong S, He Q. IEEE Signal Process Mag 1996;13:22–37.
[46] Deb K. Multi-Objective optimization using evolutionary algorithms. John Wiley & Sons; 2001.
[47] Coello CC, Lamont GB, van Veldhuizen DA. Evolutionary algorithms for solving multi-objective problems. Springer Science & Business Media; 2007.
[48] Mathworks. Global optimization toolbox, user's guide, version 3. Mathworks; 2015.
[49] Man KF, Tang KS, Kwong S. IEEE Trans Ind Electron 1996;43:519–34.

Jonathan Abir received a B.Sc. (*cum laude*) degree in mechanical engineering from Ben-Gurion University, Beer-Sheva, Israel in 2008, and a M.Sc. degree in mechanical engineering from the Technion, Haifa, Israel in 2013. He is currently working toward a Ph.D. degree at the Center for Innovative Manufacturing in Ultra-Precision, Cranfield University, Cranfield, UK. From 2008 to 2013, he was engaged in research and development of opto-mechanical systems for the defense sector, where he was awarded for his innovative and creative work.

Paul Morantz is a Principal Research Fellow in the Precision Engineering Institute at Cranfield University. He is an expert in precision metrology and has devised the mathematical bases for the complex tool-path and metrology techniques utilized across a wide range of platforms. He has extensive academic research interests and industrial experience in ultra-precision control, metrology and machine design.

Stefano Longo is a Lecturer (assistant professor) in Vehicle Electrical and Electronic Systems at Cranfield University, a Senior Member of the IEEE and a Chartered Engineer. He is the recipient of the 2011 IET Doctoral Dissertation prize for "significant achievements in the area of Control and Automation" and an Honorary Research Associate at Imperial College London. He received his M.*Sc*. in control systems from the University of Sheffield, UK, in 2007 and completed his Ph.D. in control systems at the University of Bristol, UK, in 2011. In November 2010, he was appointed to the position of research associate at Imperial College London. He joined Cranfield University in the summer of 2012.

Paul Shore was born in Chester, England, trained as machine tool designer prior to studying at Liverpool Polytechnic and then undertaking MSc and Ph.D. in Precision Engineering from Cranfield University, Cranfield, UK. From 1994 to 2002, he worked for SKF Group in the Netherland and Sweden where he managed the development of precision production systems. In 2002 he returned to Cranfield as the McKeown Professor of Ultra Precision Technologies and headed their Precision Engineering Institute where he span out Loxham Precision Limited. He was elected a Fellow of the Royal Academy of Engineering in 2009. In 2015 he became the head of Engineering Divisions at the UK's National Physical Laboratory, London.